BIFURCATION ANALYSIS OF A SPATIALLY EXTENDED LASER WITH OPTICAL FEEDBACK

KIRK GREEN*, BERND KRAUSKOPF†, FRANK MARTEN*,†, AND DAAN LENSTRA‡

Abstract. Vertical cavity surface emitting lasers (VCSELs) are a new type of semiconductor laser, characterized by the spatial extent of their disk-shaped output apertures. As a result, a VCSEL supports several optical modes (patterns of light) transverse to the direction of light propagation. When any laser is coupled to other optical elements there is unavoidable optical feedback via reflecting surfaces, which influences the stability of the laser output. For a VCSEL, the question is how the transverse optical modes interact dynamically in the presence of optical feedback and how this affects stability of the system.

In this paper, we start from a partial differential equation description of the VCSEL. We proceed by using an expansion in suitable eigenfunctions to resolve the spatial dependence. In the presence of optical feedback we obtain a model in the form of a system of delay differential equations (DDEs). As we show with the example of a VCSEL that supports two transverse modes, the spatially expanded DDE model is small enough to allow for a multi-parameter bifurcation analysis with numerical continuation tools. Specifically, we present stability regions of steady states and periodic solutions in dependence on the feedback strength and a homotopy parameter that models the amount of self- versus cross-feedback between the two modes. Bifurcations of more complicated spatio-temporal mode dynamics are then discussed.

Key words. Partial differential equation with delay; eigenfunction expansion; vertical-cavity surface-emitting semiconductor laser; VCSEL; numerical continuation

AMS subject classifications. 37N20, 34K18, 37G10, 37G20

1. Introduction. Modern semiconductor lasers combine a small size, with dimensions of a few micrometers, with a high efficiency of turning electrical energy into coherent light. Their most common applications are as light sources in optical fiber networks and as read/write systems in optical storage systems. Semiconductor lasers are also found in laser printers, sensors, scanners and even in medical applications, such as laser eye correction and dentistry. The most common semiconductor lasers today are edge-emitting lasers (EEL), where light is produced in an active region in the shape of a one-dimensional waveguide. The light travels in the plane of the chip on which the EEL is fabricated and exits at one or both end facets, which act as semi-transparent mirrors. Due to their elongated geometry, EELs generally exhibit single transverse mode lasing, which means that a single spot of light exits the laser under any operating conditions. However, an EEL may support several longitudinal modes in the direction of lasing. To ensure single longitudinal mode operation internal frequency selective elements are included in the design of some EELs.

We are concerned here with vertical cavity surface emitting lasers (VCSELs) – a second and increasingly important type of semiconductor laser. VSCELs have a cylindrical geometry, where a very thin, spatially extended active region is located in-between two stacks of mirrors; see Fig. 1. Electrical pumping via circular contacts ensures lasing in a core region. Light exits the VCSEL at a circular aperture in the top face. VCSELs are even more efficient than EELs and produce light already above a threshold current of typically only around 1 mA. They are easily coupled to optical

*Theoretical Physics, Vrije Universiteit, De Boelelaan 1081, 1081HV Amsterdam, The Netherlands (k.green@few.vu.nl);

†Department of Engineering Mathematics, University of Bristol, Bristol BS8 1TR, UK;

‡Faculty of Electrical Engineering, Mathematics and Computer Science, Delft University of Technology, Mekelweg 4, 2628 CD Delft, The Netherlands.

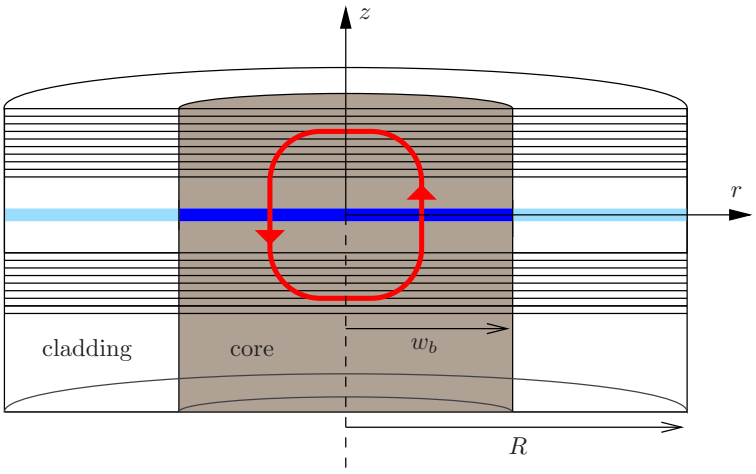

FIG. 1. *Schematic of a VCSEL showing the dielectric cylindrical waveguide approximation of an active region (blue) in the core that is surrounded by a layer of cladding. The light is reflected in between two mirror stacks and exits at the top face of the core.*

fibers and, in contrast to EELs, can be arranged on-chip into larger arrays or optical circuits. Because their active region is very thin in the direction of lasing, VCSELs provide consistent single longitudinal mode operation. From an applications point of view, the only downside is that VCSELs may lase at several transverse optical modes, which are different 'patterns of light' forming on the spatially extended disk-shaped output surface [4]. The number of optical transverse modes that a VCSEL supports increases with the diameter of the aperture. Increasing the diameter of the aperture is the main option to increase the overall output power level of the VCSEL. We note that an alternative approach would be to increase the number of quantum wells in the active layer [46].

It is now well established that semiconductor lasers are very susceptible to external optical influences; see, for example, Refs. [22, 25] as entry points to the extensive literature. In particular, even very small amounts of optical feedback in the form of back-reflected light, on the order of 0.1%, may destabilize the laser [11, 31]. This is why expensive optical isolators must be employed when the laser is coupled to other optical elements in practical applications. A semiconductor laser can be described in a rate equation approach by differential equations for the evolution of the electric field and the density of charge carriers. In the presence of optical feedback the electric field is coupled back to itself after a single fixed delay τ, which is simply the travel time from the laser to the mirror and back. For the case of a longitudinal single-mode EEL, one employs the famous Lang-Kobayashi (LK) equations [28], which have been shown in numerous studies to describe experimental measurements very well (for weak to moderate feedback); see, for example, Refs. [11, 19, 20]. From the mathematical point of view, the LK equations, and indeed other mathematical models of EEL systems with delayed optical feedback, take the form of delay differential equations (DDEs) with a fixed delay of moderate size (from three up to, say, six equations). The analysis of a DDE is complicated by the fact that it has an infinite-dimensional phase space [5, 17]. Numerical continuation tools for DDEs that allow one to find and follow equilibria, periodic solutions and their bifurcations have become available only quite recently [7, 40, 41]. The desire to understand the dynamics of laser systems with

delayed feedback has been one of the driving forces behind the development of these numerical tools [9, 12, 13, 16, 24, 38].

This paper is concerned with the dynamics of a VCSEL with optical feedback. The new element here is the spatial extent of the VCSEL: its two-dimensional lasing aperture gives rise to different transverse optical modes that interact with each other in the presence of optical feedback. Due to their transverse spatial nature, VCSELs need to be described by partial differential equations for the electric field and the carrier density. In the presence of optical feedback one is therefore dealing with a mathematical model in the form of delayed partial differential equations (DPDEs). Note that DPDE models are presently also of interest in other application areas, including the control of spatial patterns [42] and dynamics testing methods for mechanical systems [27]. To analyze or even simulate a DPDE model one generally resolves the spatial part of the system with a suitable expansion method (for example, by spatial discretization or Galerkin projection). After truncation this leads to a system of DDEs. The problem is that numerical continuation tools are not able to cope with the resulting system of DDEs if it is too large. In particular, calculating stability information of equilibria and periodic orbits is extremely time consuming and restricted by the underlying software platform.

The key is therefore to exploit physical properties of the VCSEL in order to obtain a sufficiently small system of DDEs that still describes the spatio-temporal dynamics of the transverse modes under the influence of optical feedback. We follow here the standard modeling approach of expanding the spatial electric field in a hierarchy of transverse, linearly polarized (LP) optical modes inside the cylindrical core of the VCSEL [14, 29, 44]; one also speaks of an index guided VCSEL [33]. The number of LP modes necessary for an accurate description of the VCSEL increases with the size of the aperture. Expansion in LP modes leads to a system of ordinary differential equations, one for the electric field of each mode. In the presence of an external mirror, each transverse mode is subject to delayed optical feedback from itself and from other transverse modes. The overall DPDE then takes the form of a system of DDEs for the electric fields that are coupled to a PDE for the carrier distribution in the disk-shaped active region. Carriers, provided by electrical pumping, diffuse into the active region. This type of model has been simulated numerically by discretizing the PDE for the spatial charge carriers with a finite difference scheme [29, 43, 44].

We show here that a much smaller, spatially resolved DDE model can be obtained by expanding the carrier density in the active region of the VCSEL in orthogonal eigenfunctions that satisfy the diffusion equation for the carrier distribution. A similar approach was first taken by Moriki et al. [34], but the use of a finite difference scheme has proved to be the more popular method [44]. A recent return to eigenfunction expansion methods can be found as part of the simulation package `VISTAS` by Jungo et al. [21]; however, their choice of expansion functions introduces a singularity at the origin (the center) of the VCSEL. A further advantage of eigenfunction expansions is that the overlap integrals describing the coupling between the optical modes appear as constants that need to be computed only once. This results in a substantial increase in computational efficiency, so that a multi-parameter bifurcation analysis now becomes feasible.

As a specific example we consider here the case of a VCSEL in which the first two, rotationally symmetric, LP modes are excited and demonstrate that the resulting spatially expanded DDE system is small enough to be amenable to a full numerical bifurcation analysis. The optical feedback terms are modeled in a general form as

introduced in Ref. [14], where a homotopy parameter allows us to investigate the influence of the relative amount of self- versus cross-feedback of the modes. Note that all previous studies, for example, Refs. [29, 43, 44] assumed pure self-feedback. We use the continuation package `DDE-BIFTOOL` [7] to study the the bifurcations of steady-state solutions of the VCSEL model; they are called external cavity modes (ECMs) and correspond to solutions where the two fields lase with constant intensities. The accuracy of the spatially expanded model is demonstrated by a comparison with the ECM structure given in Ref. [14], obtained with a finite difference scheme discretization of the carrier PDE. A further bifurcation analysis for the difference scheme discretized model proved entirely unpractical. On the other hand, the spatially expanded DDE model of this study provides such a considerable speed-up in the stability calculations that it is now possible to compute stability regions of ECMs in the plane of feedback strength κ and self- versus cross-feedback parameter η. What is more, we are able to continue periodic solutions that are born in Hopf bifurcations of ECMs with the numerical package `PDDE-CONT` [40]. This reveals large stability regions of periodic solutions in the (κ, η)-plane. We find two types of oscillations: in-phase oscillations of both modes at the characteristic relaxation oscillation frequency of the VCSEL, and anti-phase oscillations where the two modes suppress each other with a period given by a multiple of the external round trip time. We also consider how these periodic solutions bifurcate to quasiperiodic and even chaotic spatio-temporal dynamics of the two modes. In other words, the bifurcation analysis presented here reveals the influence of the self- versus cross-coupling parameter η on the dynamics of the spatial modes.

This paper is organized as follows. In Section 2 we introduce the general spatially-extended PDE description of the VCSEL and show how it can be reduced by a suitable mode expansion. The specific mode-expanded DDEs for the two-mode VCSEL with optical feedback are given in Section 2.4. The stability regions of the ECMs are presented in Section 3, and those of the bifurcating periodic orbits in Section 4. Bifurcations to more complicated spatio-temporal dynamics are discussed briefly in Section 5. Finally, in Section 6 we draw conclusions and point to future work.

2. Rate equation model of a VCSEL. A VCSEL with multiple transverse modes can be described in the semi-classical framework by so-called rate equations for the slowly varying complex amplitudes $E^j_{mn}(t)$ of the contributing transverse modes and for the spatially extended inversion $N(r, \phi, t)$ [44, 46]. Here the profile Ψ^j_{mn} of the mnth optical mode of polarization j is a fixed solution of the Helmholtz equation (which in turn is derived from Maxwell's equations) of the cold (not electrically pumped) laser cavity [46]. The inversion is the spatial distribution of the number of electron-hole pairs in the circular active region and, hence, it is expressed in polar coordinates for convenience. In dimensionless form the VCSEL rate equations are

given as [14]

$$\frac{dE^j_{mn}(t)}{dt} = (1+i\alpha)\xi^j_{mn}(t)E^j_{mn}(t) + F^j_{mn}(t) \tag{2.1}$$

$$\begin{aligned} T\frac{\partial N(r,\phi,t)}{\partial t} &= \frac{d_f}{r}\left[\frac{\partial}{\partial r}\Big(r\frac{\partial N(r,\phi,t)}{\partial r}\Big)\right] + \frac{d_f}{r^2}\frac{\partial^2 N(r,\phi,t)}{\partial \phi^2} + P(r,\phi,t) - N(r,\phi,t) \\ &\quad - \sum_n \Bigg((1+2\xi_{0n}(t))|E_{0n}(t)|^2 |\Psi_{0n}(r,\phi)|^2 \\ &\quad + \sum_m \sum_{j=c,s} 2(1+2\xi^j_{mn}(t))|E^j_{mn}(t)|^2 |\Psi^j_{mn}(r,\phi)|^2 \Bigg). \end{aligned} \tag{2.2}$$

Material properties of the VCSEL include the line-width enhancement factor α, the ratio between carrier and photon lifetimes T, a diffusion coefficient d_f, and a spatial pump profile P; see below. For reference, time is rescaled with respect to a photon lifetime of $\tau_p = 2$ ps. The function $F^j_{mn}(t)$ represents an external influence on the respective transverse mode that depends on its own set of parameters, such as the feedback strength. Specifically, we consider here optical feedback as introduced in Sec. 2.4 below. Note, however, we that $F^j_{mn}(t)$ could just as easily represent optical injection [30]. The equations for the different transverse optical modes are coupled via the spatial overlaps between the optical modes and the inversion, which are expressed by the modal gain integrals

$$\xi^j_{mn}(t) = \frac{\int_0^1 \int_0^{2\pi} |\Psi^j_{mn}(r,\phi)|^2 N(r,\phi,t) r dr d\phi}{\int_0^1 \int_0^{2\pi} |\Psi^j_{mn}(r,\phi)|^2 r dr d\phi}. \tag{2.3}$$

Physically, these integrals represent the competition of each spatial mode for the reservoir $N(r,\phi,t)$ of carriers. Note that Eq. (2.1) does not contain terms involving the frequencies of the individual optical modes, because they differ only on the scale of terahertz. For the case of two optical modes as considered in this paper one can transform to an electric field frame of reference with respect to the frequency difference between the two modes. If more transverse modes are present, then it is argued in Ref. [43] that Eq. (2.1) represents a first-order approximation, and that these small frequency differences may be treated as a perturbation.

2.1. Spatial optical modes. We adopt the linearly polarized (LP) description for the optical modes. This simplification of the full set of transverse magnetic, transverse electric and hybrid modes for a cylindrical waveguide is valid under the condition of weak guidance [46]. In other words, we consider a VCSEL in which the dielectric constant in the core region is approximately equal to that in the cladding region; see Fig. 1. The LP mode profiles Ψ^j_{mn} are given by roots of the Helmholtz equation [44, 46]

$$\frac{\partial^2 \Psi^j_{mn}(r,\phi)}{\partial r^2} + \frac{1}{r}\frac{\partial \Psi^j_{mn}(r,\phi)}{\partial r} + \frac{1}{r^2}\frac{\partial^2 \Psi^j_{mn}(r,\phi)}{\partial \phi^2} + q_n^2 \Psi^j_{mn}(r,\phi), \tag{2.4}$$

where

$$q_n^2 \equiv \begin{cases} u_n^2 = \epsilon^{\text{core}}\kappa_n^2 - \beta^2 & r \le a \\ w_n^2 = \beta^2 - \epsilon^{\text{clad}}\kappa_n^2 & r > a, \end{cases} \tag{2.5}$$

and ϵ^{core} and ϵ^{clad} are the dielectric constants inside the core and cladding regions, respectively. We remark that, due to changes in the inversion, the dielectric constants may vary slightly when the VCSEL is lasing. However, these variations are two orders of magnitude lower than their fixed values and, as is common in the literature, we treat ϵ^{core} and ϵ^{clad} as constants. The other parameters are the radius a of the active (core) region of the VCSEL, modal vacuum-wavenumbers κ_n, and the longitudinal wavenumber β (which is a separation of variables constant).

Solutions of Eq. (2.4) take the form

$$\Psi_{mn}^{j=c,s}(r,\phi) = \Psi_{mn}(r) \times \begin{cases} \sin(m\phi) & j = s \\ \cos(m\phi) & j = c \\ 1 & m = 0, \end{cases} \tag{2.6}$$

where

$$\Psi_{mn}(r) = \begin{cases} \dfrac{J_m(u_n r/a)}{J_m(u_n)} & r \le a \\ \dfrac{K_m(w_n r/a)}{K_m(w_n)} & r > a. \end{cases} \tag{2.7}$$

In other words, radial solutions are given by Bessel functions of the first kind J_m inside the core region ($r \le a$) and modified Bessel functions of the second kind K_m inside the cladding region ($r > a$). These solutions conform to the physical structure of the VCSEL, that is, the J_m remain finite with zero slope at $r = 0$, and the K_m for $r > a$ remain finite and rapidly decay to zero with r. Furthermore, continuity is assured at the boundary $r = a$. Their azimuthal dependence is given in terms of orthogonal sine and cosine functions, which are denoted by the superscript j.

Figure 2 shows the cosine orientated LP mode profiles $\Psi_{mn}^{c}(r,\phi)$ for $0 \le m \le 3$ and $1 \le n \le 4$ in projection onto the (r,ϕ)-plane. (A rotation over 90 degrees yields the sine orientated LP modes $\Psi_{mn}^{s}(r,\phi)$.) Here dark red corresponds to regions of high intensity and dark blue to regions of low intensity. From column to column the radial order n of the mode increases from $n = 1$ to $n = 4$; note that n represents the number of peaks in the radial mode profiles counted from the origin outwards. From row to row the azimuthal order m of the mode increases from $m = 0$ to $m = 3$; note that $2m$ represents the number of dark sectors over one full rotation.

2.2. Expansion of the angular dependence. To make Eqs. (2.1) and (2.2) amenable to a full nonlinear bifurcation analysis with numerical tools such as `DDE-BIFTOOL` [7] and `PDDE-CONT` [40], we now resolve the spatial dependence by expansion in suitable basis functions. A common first step [44] is to expand the angular part of the inversion $N(r,\phi,t)$ as a Fourier series

$$N(r,\phi,t) = \sum_{k=0}^{\infty} \big(N_{ck}(r,t) cos(k\phi) + N_{sk}(r,t) sin(k\phi) \big). \tag{2.8}$$

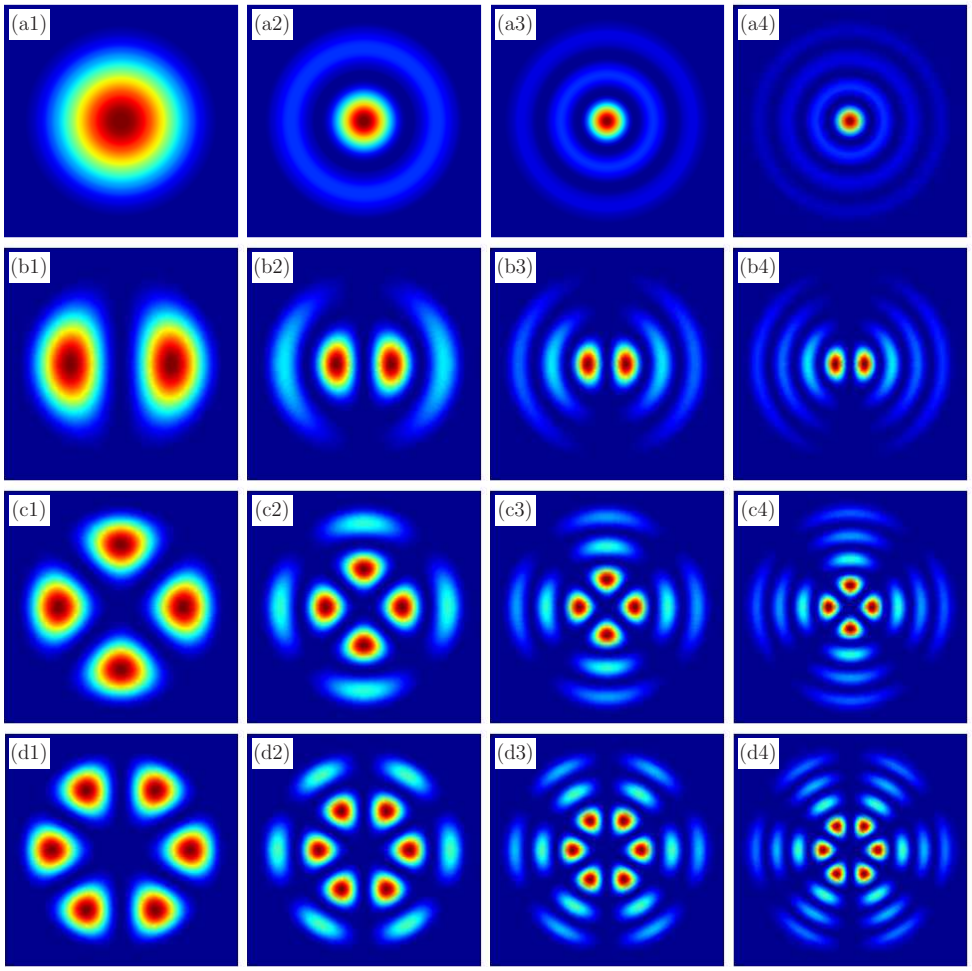

FIG. 2. *The linearly polarized optical modes LP_{mn} for $0 \leq m \leq 3$ and $1 \leq n \leq 4$; the index m changes from row to row and the index n from column to column.*

The resulting set of rate equations are premultiplied by both $\sin(k\phi)$ and $\cos(k\phi)$, and integrated over ϕ, to obtain the following system of PDEs

$$\frac{dE^j_{mn}}{dt} = (1+i\alpha)\xi^j_{mn}E^j_{mn} + F^j_{mn}(t), \tag{2.9}$$

$$T\frac{\partial N_{c0}(r,t)}{\partial t} = \frac{d_f}{r}\frac{\partial}{\partial r}\Big(r\frac{\partial N_{c0}}{\partial r}\Big) + \int_0^{2\pi}\frac{P(r,\phi,t)}{2\pi}\,d\phi - N_{c0} \tag{2.10}$$
$$- \sum_n \left((1+2\xi_{0n})|E_{0n}|^2|\Psi_{0n}|^2 - \sum_m \sum_{j=c,s} (1+2\xi^j_{mn})|E^j_{mn}|^2|\Psi_{mn}|^2 \right),$$

$$T\frac{\partial N_{ck}(r,t)}{\partial t} = \frac{d_f}{r}\frac{\partial}{\partial r}\Big(r\frac{\partial N_{ck}}{\partial r}\Big) - \frac{d_f}{r^2}k^2N_{ck} + \int_0^{2\pi}\frac{P(r,\phi,t)}{\pi}\cos(k\phi)\,d\phi - N_{ck}$$
$$- \sum_m\sum_n |\Psi_{mn}|^2\delta_{(2m)k}((1+2\xi^c_{mn})|E^c_{mn}|^2 - (1+2\xi^s_{mn})|E^s_{mn}|^2), \tag{2.11}$$

$$T\frac{\partial N_{sk}(r,t)}{\partial t} = \frac{d_f}{r}\frac{\partial}{\partial r}\Big(r\frac{\partial N_{sk}}{\partial r}\Big) - \frac{d_f}{r^2}k^2N_{\xi k} + \int_0^{2\pi}\frac{P(r,\phi,t)}{\pi}\sin(k\phi)\,d\phi - N_{sk}, \tag{2.12}$$

where $\delta_{(2m)k}$ is the Kronecker symbol meaning that $\delta_{(2m)k} = 1$ for $2m = k$ and $\delta_{(2m)k} = 0$ otherwise. The modal gains $\xi^j_{mn}(t)$ are now given as

$$\xi_{0n}(t) = \int_0^1 |\Psi_{0n}(r)|^2 N_{c0}(r,t) r dr,$$

$$\xi^c_{mn}(t) = \int_0^1 |\Psi_{mn}(r)|^2 \Big(N_{c0}(r,t) + \frac{1}{2}\sum_{k=1}^{\infty} \delta_{(2m)k} N_{ck}(r,t) \Big) r dr,$$

$$\xi^s_{mn}(t) = \int_0^1 |\Psi_{mn}(r)|^2 \Big(N_{c0}(r,t) - \frac{1}{2}\sum_{k=1}^{\infty} \delta_{(2m)k} N_{ck}(r,t) \Big) r dr.$$

We assume that the pump current is rotationally symmetric and constant in time, so that $P(r,\phi,t) \equiv P(r)$ and

$$\int_0^{2\pi} \frac{P(r)}{2\pi}\, d\phi = P(r)$$

in Eq. (2.10) and

$$\int_0^{2\pi} \frac{P(r)}{\pi} \cos(k\phi)\, d\phi = \int_0^{2\pi} \frac{P(r)}{\pi} \sin(k\phi)\, d\phi = 0$$

in Eqs. (2.11) and (2.12).

Finally, we note that for $k \neq 2m$, Eq. (2.11) is homogeneous. Moreover, under the assumption of a symmetric pump current, Eq. (2.12) is always homogeneous and, thus, the two-dimensional PDE describing the inversion is reduced to the following system of PDEs with a one-dimensional radial dependence:

$$\frac{dE^j_{mn}}{dt} = (1 + i\alpha)\xi^j_{mn} E^j_{mn} + F^j_{mn}(t), \tag{2.13}$$

$$\begin{aligned} T\frac{\partial N_0(r,t)}{\partial t} &= d_f \left[\frac{1}{r}\frac{\partial}{\partial r}\Big(r \frac{\partial N_0}{\partial r} \Big) \right] + P(r) - N_0 \\ &\quad - \sum_n \left((1 + 2\xi_{0n}) |E_{0n}|^2 |\Psi_{0n}|^2 - \sum_m \sum_{j=c,s} (1 + 2\xi^j_{mn}) |E^j_{mn}|^2 |\Psi_{mn}|^2 \right), \end{aligned} \tag{2.14}$$

$$\begin{aligned} T\frac{\partial N_k(r,t)}{\partial t} &= d_f \left[\frac{1}{r}\frac{\partial}{\partial r}\Big(r \frac{\partial N_k}{\partial r} \Big) \right] - \frac{d_f}{r^2} k^2 N_k - N_k \\ &\quad - \sum_m \sum_n |\Psi_{mn}|^2 \delta_{(2m)k} ((1 + 2\xi^c_{mn}) |E^c_{mn}|^2 - (1 + 2\xi^s_{mn}) |E^s_{mn}|^2), \end{aligned} \tag{2.15}$$

where, for ease of presentation, we have written $N_k \equiv N_{ck}$, $k = 0, 2, 4, ...$

It is clear that the number of terms of the expansion that we need to keep depends on the number of optical modes we wish to consider. Here the *azimuthal orders* of these modes are given by the index m. For example, for a VCSEL which only supports rotationally symmetric modes $m = 0$ (Fig. 2 row (a), and the case we will consider later), Eq. (2.15) is not needed nor is the last, double summation term of Eq. (2.14). In this way, we are left with a single PDE with a one-dimensional radial dependence describing the inversion. Likewise, for a VCSEL supporting both rotationally symmetric and first-order azimuthal modes $m = 0, 1$ (recall Fig. 2 rows (a) and (b)), we need two PDEs $\partial N_0(r,t)/\partial t$ and $\partial N_2(r,t)/\partial t$ for a full description. It follows that a system of $(M + 1)$ PDEs, with one-dimensional radial dependencies, describe VCSELs which support modes up to a Mth azimuthal order.

2.3. Expansion of the radial dependence. In the literature, the most common way of dealing with the radial PDEs (2.14) and (2.15) is through the use of a finite difference discretization scheme [14, 44]. This approach works well for rotationally symmetric modes [14]. However, it runs into problems for modes with $m > 0$. Specifically, the $1/r^2$ term in Eq. (2.15) introduces a singularity at $r = 0$. This singularity is generally avoided by not placing a mesh point of the finite difference scheme at $r = 0$; accuracy of this approach is typically tested by comparing results for increasingly smaller mesh intervals as $r \to 0$ [44].

A second method for arriving at a spatially resolved model is to expand the radially dependent inversion in terms of another set of orthogonal functions. As the optical modes are written in terms of Bessel functions, it has been proposed to use such a set of functions in which to expand the radially dependent inversion [21, 34]. In particular, the computation package `VISTAS` [21] employs the use of *zeroth order* Bessel functions of the first kind. However, we note that this expansion still leaves terms depending on $1/r$. Thus, the singularity problem at $r = 0$ is unresolved. (Again, `VISTAS` avoids computing values at $r = 0$.)

In this paper, we take a more general approach. Namely, we expand each inversion coefficient $N_k(r, t)$ in terms of a *kth order* Bessel function expansion of the first kind,

$$N_k(r,t) = \sum_{q=1}^{\infty} N_{kq}(t) J_k(\gamma_{k,q} r), \tag{2.16}$$

where the $\gamma_{k,q}$ are roots of J_k. In this way, noting the scaling of the Bessel function arguments, the boundary conditions of the PDE problem [14] are matched; that is, $\frac{\partial N_k(0,t)}{\partial r} = 0$ and $N_k(1, t) = 0$.

Most importantly, the kth order Bessel functions $J_k(\gamma_{k,q} r)$ are exact eigenfunctions of the kth order operators

$$\nabla_k^2 \equiv \frac{1}{r}\frac{\partial}{\partial r}\Big(r\frac{\partial}{\partial r}\Big) - \frac{k^2}{r^2}, \tag{2.17}$$

which appear in Eqs. (2.14) and (2.15). We proceed by inserting the expansion (2.16) into Eqs. (2.14) and (2.15), multiplying each of the expanded rate equations for N_k by a corresponding $rJ_k(\gamma_{k,l} r)$, and integrating over r. Thus, through the orthogonality condition

$$\int_0^1 J_k(\gamma_{k,q} r) J_k(\gamma_{k,l} r) r dr = \frac{\delta_{ql}}{2}[J_{k+1}(\gamma_{k,l})]^2, \tag{2.18}$$

one obtains the following set of *spatially resolved* rate equations

$$\frac{dE_{mn}^j(t)}{dt} = (1 + i\alpha)\xi_{mn}^j E_{mn}^j + F(t) \tag{2.19}$$

$$\begin{aligned} T\frac{dN_{0q}(t)}{dt} &= -(\gamma_{0,q}^2 d_f + 1)N_{0q} + \rho_q \\ &\quad - \sum_n \left((1 + 2\xi_{0n})|E_{0n}|^2 \beta_{0n}^{0q} + \sum_m \sum_{j=c,s} (1 + 2\xi_{mn}^j)|E_{mn}^j|^2 \beta_{mn}^{0q} \right), \end{aligned} \tag{2.20}$$

$$\begin{aligned} T\frac{dN_{kq}(t)}{dt} &= -(\gamma_{k,q}^2 d_f + 1)N_{kq}(t) \\ &\quad - \sum_m \sum_n \delta_{(2m)k} \left((1 + 2\xi_{mn}^c)|E_{mn}^c|^2 - (1 + 2\xi_{mn}^s)|E_{mn}^s|^2 \right) \beta_{mn}^{kq}, \end{aligned} \tag{2.21}$$

where the two integrals

$$\rho_q = \frac{2}{[J_1(\gamma_{0,q})]^2} \int_0^1 P(r) J_0(\gamma_{0,q} r)\, r dr, \tag{2.22}$$

$$\beta_{mn}^{kq} = \frac{2}{[J_{k+1}(\gamma_{k,q})]^2} \int_0^1 |\Psi_{mn}(r)|^2 J_k(\gamma_{k,q} r)\, r dr, \tag{2.23}$$

describe the spatial overlaps between the inversion density with the pump current and the electric field, respectively. These integrals depend on the material properties and geometry of the VCSEL model under consideration. Furthermore, the modal gains are now given as

$$\xi_{0n} = \sum_{q=1}^{\infty} \int_0^1 \left(|\Psi_{0n}(r)|^2 N_{0q} J_0(\gamma_{0,q} r) \right) r dr, \tag{2.24}$$

$$\xi_{mn}^c = \sum_{q=1}^{\infty} \int_0^1 |\Psi_{mn}(r)|^2 \left(N_{0q} J_0(\gamma_{0,q} r) + \frac{1}{2} \sum_{k=1}^{\infty} \delta_{(2m)k} N_{kq} J_k(\gamma_{k,q} r) \right) r dr, \tag{2.25}$$

$$\xi_{mn}^s = \sum_{q=1}^{\infty} \int_0^1 |\Psi_{mn}(r)|^2 \left(N_{0q} J_0(\gamma_{0,q} r) - \frac{1}{2} \sum_{k=1}^{\infty} \delta_{(2m)k} N_{kq} J_k(\gamma_{k,q} r) \right) r dr. \tag{2.26}$$

Importantly, the integrals above need to be evaluated only once and then appear as constants. Hence, their evaluation does not add to the overall computation time.

In practice, the Bessel function expansion (2.16) will have to be truncated at some finite order. The arguments for this truncation are more subtle than for the Fourier expansion (2.8). Clearly, there is no upper bound for the sum in Eq. (2.16). However, we can consider the time scale at which the higher-order terms in the expansion $N_{kq}(t)$ are damped. Specifically, this timescale is given by the first term in the right-hand side of Eqs. (2.20) and (2.21) as

$$\tau_{kq} = \frac{1}{1 + \gamma_{k,q}^2 d_f}. \tag{2.27}$$

As the values of $\gamma_{k,q}^2$ increase with q, the higher order terms $N_{kq}(t)$ tend to zero. The convergence of solutions for increasing terms in the Bessel function expansion can also be tested numerically.

2.4. Reduced model of a two-mode VCSEL with optical feedback. We are concerned here with a VCSEL that is subject to delayed optical feedback from an external mirror. While this question can be studied, in principle, for any number of modes with the truncated rate equation model presented above, we consider here the case that the VCSEL supports the first two optical modes LP_{01} and LP_{02}. Considering only these two modes is realistic; for example, control of individual modes, in a laser supporting the LP_{01} and LP_{02} modes, has been demonstrated via external injection [36]. Likewise, different modes may be selected via frequency selective feedback [32]. This two-mode set-up has been studied theoretically in Refs. [14, 43].

Importantly, the first two optical modes do not have an azimuthal component, so that they can be described by their radial dependence alone. Figure 3 shows the two radial profiles of the mode profiles $|\Psi_{01}|^2$ and $|\Psi_{02}|^2$ of the LP_{01} and LP_{02}. For the

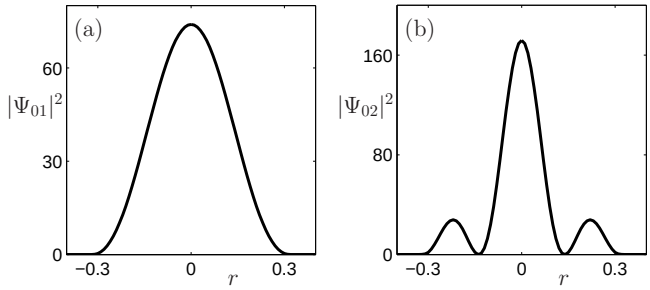

FIG. 3. *Radial profile* $|\Psi_{01}|^2$ *of the optical mode* LP_{01} *(a), and* $|\Psi_{02}|^2$ *of* LP_{02} *(b).*

two modes LP_{01} and LP_{02} the rate equations (2.19)–(2.21) reduce to

$$\frac{dE_1(t)}{dt} = (1+i\alpha)\xi_1 E_1(t) + F_1(t), \tag{2.28}$$

$$\frac{dE_2(t)}{dt} = (1+i\alpha)\xi_2 E_2(t) + F_2(t), \tag{2.29}$$

$$T\frac{dN_q(t)}{dt} = -(\gamma_{0,q}^2 d_f + 1)N_q(t) + \rho_q - \sum_{n=1}^{2}\left((1+2\xi_n)|E_n(t)|^2\beta_n^{0q}\right), \tag{2.30}$$

where, for ease of presentation, we write $E_{0n} \equiv E_n$, $\xi_{0n} \equiv \xi_n$ and $N_{0q} \equiv N_q$. Here Eqs. (2.30) are the expansion equations of the radial dependence of the inversion. We consider here a total of 14 expansion terms, that is, $q = 1 \ldots 14$, which we found guarantees a relative error of below 0.01% at the steady state solutions. The overlap integrals are now given as

$$\xi_n = \sum_{q=1}^{14}\int_0^1 \left(|\Psi_n(r)|^2 N_q J_0(\gamma_{0,q}r)\right) r dr, \tag{2.31}$$

$$\rho_q = \frac{2}{[J_1(\gamma_{0,q})]^2}\int_0^1 P(r)J_0(\gamma_{0,q}r)\, r dr, \tag{2.32}$$

$$\beta_n^{0q} = \frac{2}{[J_1(\gamma_{0,q}^2)]}\int_0^1 |\Psi_n(r)|^2 J_0(\gamma_{0,q}r)\, r dr. \tag{2.33}$$

As in Ref. [14] we consider a disc-shaped profile with pumping confined to a core region of radius 0.3 of the VCSEL, as given by

$$P(r) = P_{\max}\big(1 + \mathrm{erf}(2\sqrt{75}(-r+0.3))\big)/2. \tag{2.34}$$

The other laser parameters are fixed to the realistic values $\alpha = 3$, $T = 750$, $d_f = 0.05$, and $P_{\max} = 2$.

We are interested here in the influence of self-feedback versus cross-feedback of individual modes of the rate equation model. To this end, we need to specify the optical feedback terms F_1 and F_2 in Eqs. (2.28) and (2.29). As in Ref. [14] we consider

$$F_1(t) = \kappa e^{iC_p}\big[\eta E_1(t-\tau) + (1-\eta)E_2(t-\tau)\big], \tag{2.35}$$

$$F_2(t) = \kappa e^{iC_p}\big[\eta E_2(t-\tau) + (1-\eta)E_1(t-\tau)\big], \tag{2.36}$$

where the feedback enters with a common feedback strength κ and feedback phase C_p. The delay time is set to $\tau = 500$, which corresponds to a distance of approximately

10 cm between the laser and the mirror. The homotopy parameter η represents the amount of self-feedback versus cross-feedback. This allows the two optical modes to couple via the external cavity, that is, via the optical feedback. Indeed one would expect in general to observe a certain amount of cross-feedback; for example, the modes could easily cross-couple due to deformations in the shape of the external mirror. However, the precise amount of cross-coupling is very hard to estimate or measure. This motivates our bifurcation study with emphasis on how the cross-coupling parameter η affects the dynamics of the VCSEL over the entire range from pure self-feedback $\eta = 1$ to pure cross-feedback $\eta = 0$.

Equations (2.28)–(2.30) with (2.31)–(2.36) are a system of 18 (real-valued) delay differential equations, which provide a good approximation of the delayed PDE model of a VCSEL. This model combines a relatively small system size with the fact that the overlap integrals can be calculated a priori. Compared to the model of dimension 105 considered in Ref. [14], where the inversion equation was discretized with a second-order finite difference scheme, the model presented here offers a substantial speed-up. For example, stability calculations of steady states that took 452.46 s (7.54 minutes) per point on a branch in Ref. [14], now take only 6.41 s on a 3.4 GHz `Xeon` processor. As a consequence, we are now able to present a detailed multi-parameter bifurcation analysis of the ECMs, their stability, and even of bifurcating periodic solutions.

3. External cavity modes. The basic solutions of a laser subject to optical feedback are known as external cavity modes (ECMs), which correspond to constant intensity of the laser at a frequency that is selected by the external cavity. In other words, ECMs are due to the fact that the light makes one round trip outside the laser [28]. In the case of model (2.28)–(2.36) of a VCSEL with optical feedback the ECMs are of the form [14]

$$\big(E_1(t), E_2(t), N_q(t)\big) = (R_1 e^{i\omega_s t}, R_2 e^{i\omega_s t + i\Phi}, N_1, ..., N_Q), \tag{3.1}$$

where $R_1, R_2, \omega_s, \Phi, N_1, ..., N_Q \in \mathbb{R}$. As with other types of lasers subject to optical feedback, the ECMs are group orbits under the rotational S^1-symmetry of the governing equations [26]. In order to obtain an isolated solution that can be continued numerically we first transform Eqs. (2.28)–(2.36) to a rotating frame of reference with frequency b. By setting $b = \omega_s$ the ECMs are then found as steady state solutions; see Refs. [9, 16, 26] for further details.

The ECMs of Eqs. (2.28)–(2.36) lie on closed curves, called ECM-components, that are parametrized by the periodic parameter C_p. As C_p is varied, ECMs are born in pairs in a saddle-node bifurcation, move over the respective ECM-component, and then disappear in pairs in another saddle-node bifurcation. The ECM-components were computed in Ref. [14] with the continuation package `DDE-BIFTOOL`, where it was shown that there are several types of ECM components. There exist ECM components for which the first field E_1 is dominant, while the second field E_2 provides a negligible contribution to the total power, and vice versa. More interestingly, there exist ECM-components where both fields contribute to the total power, one of which contains stable ECMs [14].

We focus here on the latter ECM-component and study the stability of the corresponding ECMs in dependence on the feedback strength κ and on the self- versus cross-feedback parameter η. Note that κ is a common parameter to consider in the laser dynamics literature. While it is difficult to experimentally determine the exact amount of light that re-enters the laser, the feedback strength can be varied in an experiment by means of density filters. We concentrate here on the physically

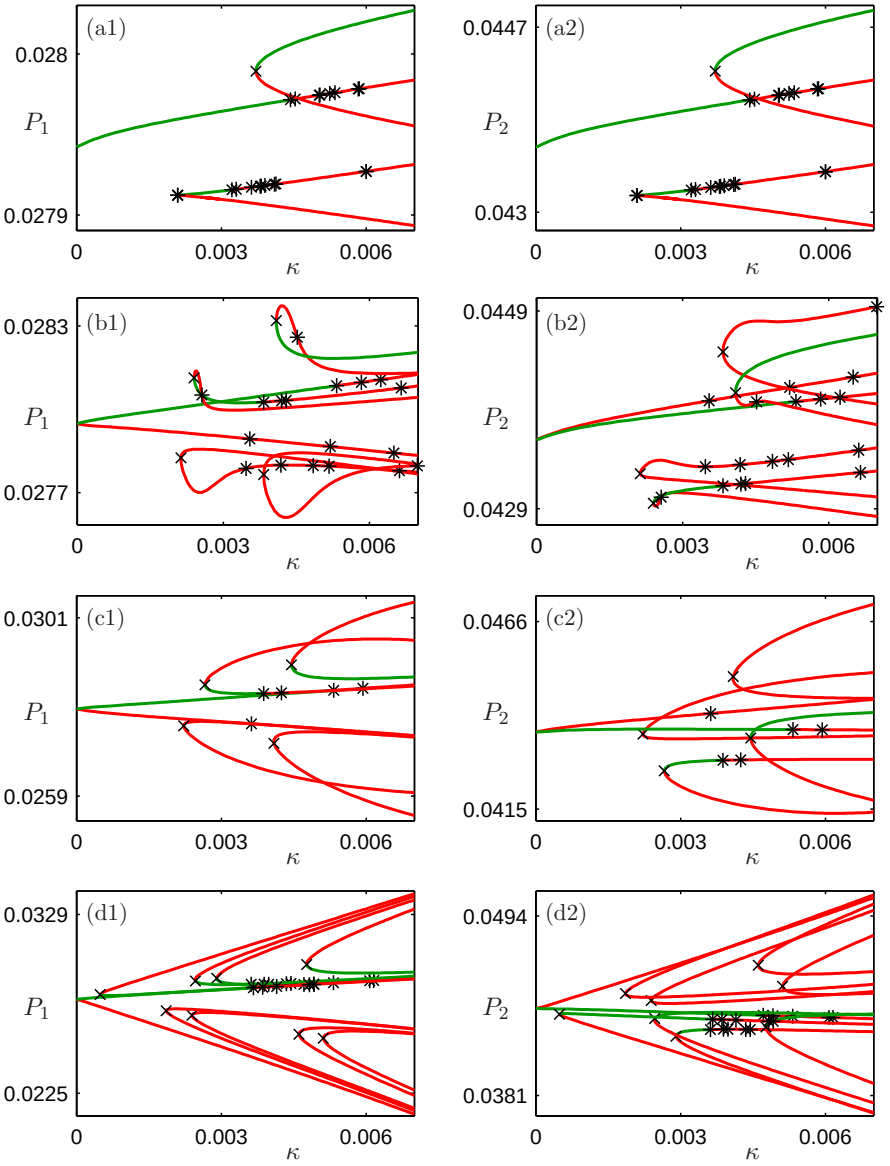

FIG. 4. *Branches of ECMs as a function of κ, shown in terms of the powers P_1 of the first mode (left) and P_2 of the second mode (right). From row (a) to (d) η takes the values 1.0, 0.9, 0.6 and 0.0, respectively; throughout $C_p = 0$.*

relevant region of weak feedback strength where $\kappa \leq 0.007$, which corresponds to a maximum of about 0.001% back-reflected light. The exact amount of self- versus cross-feedback, expressed by the parameter η, is generally not known. Nevertheless, one would certainly expect that there is some amount of cross-feedback, which would mean that $\eta < 1$. Moreover, it may be possible to tune η experimentally, for example, via external mirror shaping or frequency selective optical feedback [32]. This makes

η an ideal parameter for a bifurcation study that aims at obtaining a global view of the influence of self- versus cross-feedback over the entire possible range.

We start by computing branches of ECMs as a function of the feedback strength κ, for fixed $C_p = 0$ and several values of η. Figure 4 was obtained with `DDE-BIFTOOL` and shows ECM-branches of Eqs. (2.28)–(2.36) in the (κ, P_1)-plane (left) and the (κ, P_2)-plane (right) for $\eta = 1.0$ (row a), $\eta = 0.9$ (row b), $\eta = 0.6$ (row c), and $\eta = 0.0$ (row d). Segments of branches on which one finds stable ECMs are green, while unstable ECM-branches are red. The stability of ECMs is determined in `DDE-BIFTOOL` from the computation of right-most characteristic roots using linear multi-step methods [8, 45]. Due to the presence of a fixed delay, there are infinitely many discrete eigenvalues, but only finitely many with positive real part [5, 17]. Hence, as for ODEs, one generically finds saddle-node and Hopf bifurcations when a single parameter is changed. Apart from the ECM-branch that extends from $\kappa = 0$, additional ECMs are born in saddle-node bifurcations ($\times$) as the feedback strength κ is increased. On one of the bifurcating branches, ECMs may be initially stable but for increasing κ they lose stability in Hopf bifurcations ($*$). This general scenario is typical for a (single mode) laser with optical feedback [9, 16, 38]. The difference here is that we obtain a projection of the ECM branches for each of the two modes, as represented in Fig. 4 by the two intensities P_1 and P_2.

Figure 4 illustrates the strong influence of the self- versus cross-feedback parameter η. Namely, for $\eta = 1$, that is, for pure self-feedback, the ECM-branches in panels (a1) and (a2) are double-covered. Any small amount of cross feedback 'unfolds' this situation into twice as many ECM-branches; see Figs. 4(b1) and (b2). Notice that there is now a considerable difference in the shape of the ECM-branches of the two modes, which means physically that small changes in κ may cause both an increase or a decrease in the contribution of each mode to the total power. Decreasing η further, changes the shape of the ECM-branches; see Figs. 4(c1) and (c2). Furthermore, extra ECM-branches enter the region of feedback strength considered here, some of which may be stable; see Figs. 4(d1) and (d2).

The ECM branches in Fig. 4 for the mode-expanded model (2.28)–(2.36) agree very well with those in [14, Figs. 9 and 10] where a finite difference scheme was used for the carrier distribution N. Of crucial importance is that a stability calculation of a single, fixed ECM shown in Fig. 4 took 6.41 s on a 3.4 GHz `Xeon` processor, while the corresponding computation for the finite difference discretized model [14] took 452.46 s (7.54 minutes). This remarkable speed-up in computation time allows us to find and follow bifurcations of the ECMs in parameters, which provides a much broader insight into the stability of ECMs in the two-mode VCSEL. As we will see in Sec. 4, we are even able to continue the bifurcating periodic orbits and determine their stability regions.

3.1. Stability regions of ECMs. Figure 5 shows the curves saddle-node bifurcations (blue) and Hopf bifurcations (red) in the two-parameter (κ, η)-plane; dark red segments correspond to supercritical and light red segments to subcritical Hopf bifurcations. The bifurcations were identified in Fig. 4 and then continued in κ and η with `DDE-BIFTOOL`. Figures 5(a) to (e) are for one particular stable ECM each, whose region of stability is shaded green. The final Fig. 5(f) shows the complete ECM stability diagram in the (κ, η)-plane; namely, it is an overlay of panels (a) to (e). Here regions are shown in different shades of green to indicate how many stable ECMs coexist. Specifically, in the region with the lightest shade of green one finds a single stable ECM; for example, directly to the right of $\kappa = 0$. The next darker shade of green corresponds to regions

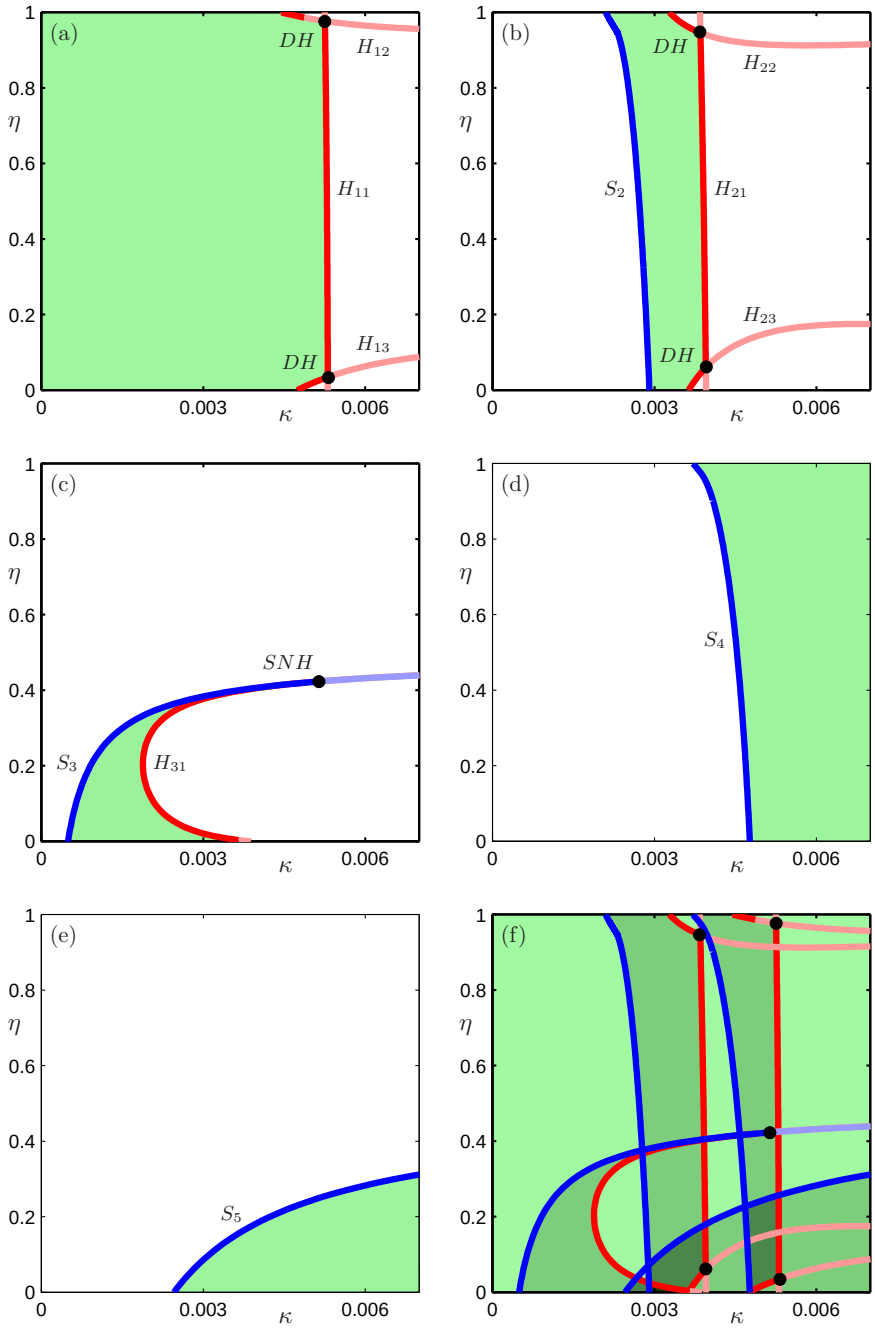

FIG. 5. *Stability regions (green) of different ECMs in the (κ, η)-plane, which are bounded by curves of saddle-node bifurcations (blue) and Hopf bifurcations (red). Panel (f) is an overlay of the different ECM stability regions in panels (a)–(e), where increasingly darker shading indicates regions of increasing multistability; throughout $C_p = 0$.*

of bistability between two ECMs; for example, directly to the right of the left-most blue saddle-node curve. The darkest shade of green corresponds to regions in which one finds three coexisting stable ECMs; note that this occurs in the region of small η, that is, for large amounts of cross-feedback. Physically, multistability between ECMs may be exploited for use in, for example, optical flip-flop schemes [23].

More specifically, it can be seen from Fig. 5(a) that a stable ECM is born at $\kappa = 0$. As κ is increased, additional stable ECMs are born in saddle-node bifurcations S_2, S_3, S_4 and S_5; see Figs. 5(b) to (e). The resulting additional stability regions lead to the large regions in Fig. 5(f) where two stable ECMs coexist. Note that some of these regions extend over the entire range of η; see, for example, Fig. 5(f) for feedback strengths of $\kappa = 0.0034$ and $\kappa = 0.0051$. Furthermore, for $(\kappa, \eta) \approx (0.006, 0.432)$ and in the range of higher values of cross-feedback, Fig. 5(c) shows an additional curve of saddle-node bifurcations entering our κ-range of interest. This curve leads to the birth of the extra (stable) ECM-branches we observed in Figs. 4(d1) and (d2). As Fig. 5(f) shows, this stable ECM leads to a main region of bistable ECMs at low values of κ and η. A second saddle-node curve enters our κ-range of interest at $\eta \approx 0.283$; see Fig. 5(e). The bifurcating stable ECMs give rise to regions in which one finds three stable ECMs; see, for example, Fig. 5(f) for $(\kappa, \eta) = (0.0035, 0.07)$ and $(\kappa, \eta) = (0.0051, 0.1)$. Finally, we note a small and barely visible region in Fig. 5(f), just above $(\kappa, \eta) = (0.0032, 0.0)$, in which one finds four coexisting, stable ECM solutions.

The stable ECMs in Figs. 5(a) to (c) are destabilized in Hopf bifurcations H_{11}, H_{12}, H_{13}, H_{21}, H_{22}, H_{23} and H_{31}, as κ is increased. For the most part, these Hopf bifurcations are supercritical (dark red curves) and lead to stable periodic solutions, which are the subject of Sec. 4. Moreover, interactions of the bifurcation curves in Fig. 5 correspond to codimension-two bifurcation points. We find four double-Hopf bifurcations DH, where two Hopf curves cross and interact. Close to these points the respective Hopf bifurcations change from supercritical (dark red) to subcritical (light red). We also find a codimension-two saddle-node Hopf bifurcation point SNH at $(\kappa, \eta) \approx (4.01 \times 10^{-3}, 0.420)$, where the Hopf curve H_{31} forms a tangency with the saddle-node curve S_3. The two curves bound the stability regions of the associated ECM, and are subcritical beyond SNH.

4. Bifurcating periodic solutions. We now address the question of what kind of stable periodic solutions may bifurcate from the different stable ECMs at the supercritical Hopf bifurcation curves shown in Fig. 5. To answer this question, we follow periodic orbits and their bifurcations with the `C++` continuation software `PDDE-CONT` [40]. Note that `PDDE-CONT` contains routines that are specifically designed to analyze systems with S^1-symmetry, such as system (2.28)–(2.36). More specifically, we first compute branches of periodic solutions emanating from the Hopf bifurcations of stable ECMs identified in Figs. 5(a) to (c). We then find and follow in the (κ, η)-plane the bifurcation curves that form the stability boundaries. Stability of periodic solutions is determined in `PDDE-CONT` from the Floquet multipliers, that is, from the eigenvalues of the Poincaré return map in a suitable transverse section. Because of the fixed delay, there is an infinite number of discrete Floquet multipliers with the origin of the complex plane as their only accumulation point [17]. Hence, as for ODEs, one generically finds saddle-node of limit cycle, period-doubling and torus (or Neimark-Sacker) bifurcations when a single parameter is changed.

Figures 6 and 7 show two examples of stable periodic solutions that bifurcate from the Hopf bifurcation curve H_{11} in Fig. 5(a) and the Hopf bifurcation curve H_{31}

in Fig. 5(c), respectively. In Figs. 6 and 7, panel (a) shows the branch of periodic solutions as it bifurcates from the corresponding Hopf bifurcation point H. The periodic solution is initially stable (green curve) and then destabilizes when κ is increased in a torus bifurcation T and a period-doubling bifurcation PD, respectively. The other panels of Figs. 6 and 7 show the periodic dynamics of a stable periodic solution in terms of the two modes, LP_{01} associated with E_1 (black) and LP_{02} associated with E_2 (gray). Specifically, panels (b1) and (b2) are time series of the powers $P_1 = |E_1|^2$ and $P_2 = |E_2|^2$ over 5 periods, panel (c) shows the projection onto the E_i-plane ($i = 1, 2$), and panel (d) that onto $(E_i, \hat{N})$-space. Here $\hat{N}$ is the mean value of the individual inversion coefficients $N_1...N_{14}$, over the orbit. Note that, because both fields feed from the same reservoir of carriers, the inversion for both fields is the same at any given time t. In panels (c) and (d) the black and the gray dot on the periodic orbit are passed at the same time in the direction indicated by the arrows. Finally, panels (e1) and (e2) show the time series of the spatial intensities $I_1 = P_1|\Psi_1|^2$ and $I_2 = P_2|\Psi_2|^2$ of the two modes.

As Figs. 6(b1) and (b2) show, for a stable periodic solution emanating from the Hopf curve H_{11} in Fig. 5(a), for $\eta = 0.6$ the two electric fields E_1 and E_2 are in phase to very good approximation. The solution moves over the crescent-shaped periodic orbits in panels (c) and (d) in a clockwise direction as indicated by the arrows. The period is approximately 75 dimensionless time units, which corresponds to a physical frequency of 6.67 GHz. This identifies the periodic solution physically as a so-called undamped relaxation oscillation (RO). Note that relaxation oscillations of a semiconductor laser are not relaxation oscillations in the sense of slow-fast systems [15]. Rather, they are a damped periodic exchange between the carriers and the electric field of a free-running semiconductor laser, which are observed when the laser is perturbed from steady operation. The spatial nature of damped relaxation oscillations has been observed experimentally with specialized measurement techniques in Refs. [1, 2]. Therefore, it may also be possible to observe the spatio-temporal dynamics of the two modes for the case of sustained, undamped ROs. The in-phase dynamics of the two modes is also apparent from the time series of the spatial intensity profiles I_1 and I_2 in Figs. 6(e1) and (e2).

By contrast, as Figs. 7(b1) and (b2) show, for a stable periodic solution emanating from H_{31} in Fig. 5(c), for $\eta = 0.2$ the two electric fields E_1 and E_2 are in approximate anti-phase. Figure 7(c) shows that the solution again moves over crescent-shaped periodic orbits in a clockwise direction as indicated by the arrows, but the two periodic orbits are now situated about π out of phase; see also panel (d). The periodic solution in Fig. 7 has a period of approximately 1512 dimensionless time units, which corresponds to a physical frequency of 331 MHz. This type of oscillation is much slower than ROs and rather takes place on the time-scale of an integer multiple of the external cavity round trip time τ. Therefore, the associated spatio-temporal dynamics of the modes should be easier to observe experimentally [1, 2]. The time series of the spatial intensity profiles I_1 and I_2 in Figs. 7(e1) and (e2) clearly show anti-phase dynamics. In other words, there is competition between the two modes, with the result that they suppress each other in the total field.

The two types of periodic solutions, in-phase ROs and anti-phase external round trip oscillations (EOs), are representative. Specifically, the solution which bifurcates from the Hopf curve H_{21} in Fig. 5(b) is an in-phase RO very similar to that shown in Fig. 6. On the other hand, solutions born at the remaining Hopf curves, H_{12}, H_{13}, H_{22} and H_{23} in Fig. 5, are in anti-phase and have periods on the order of τ. Namely,

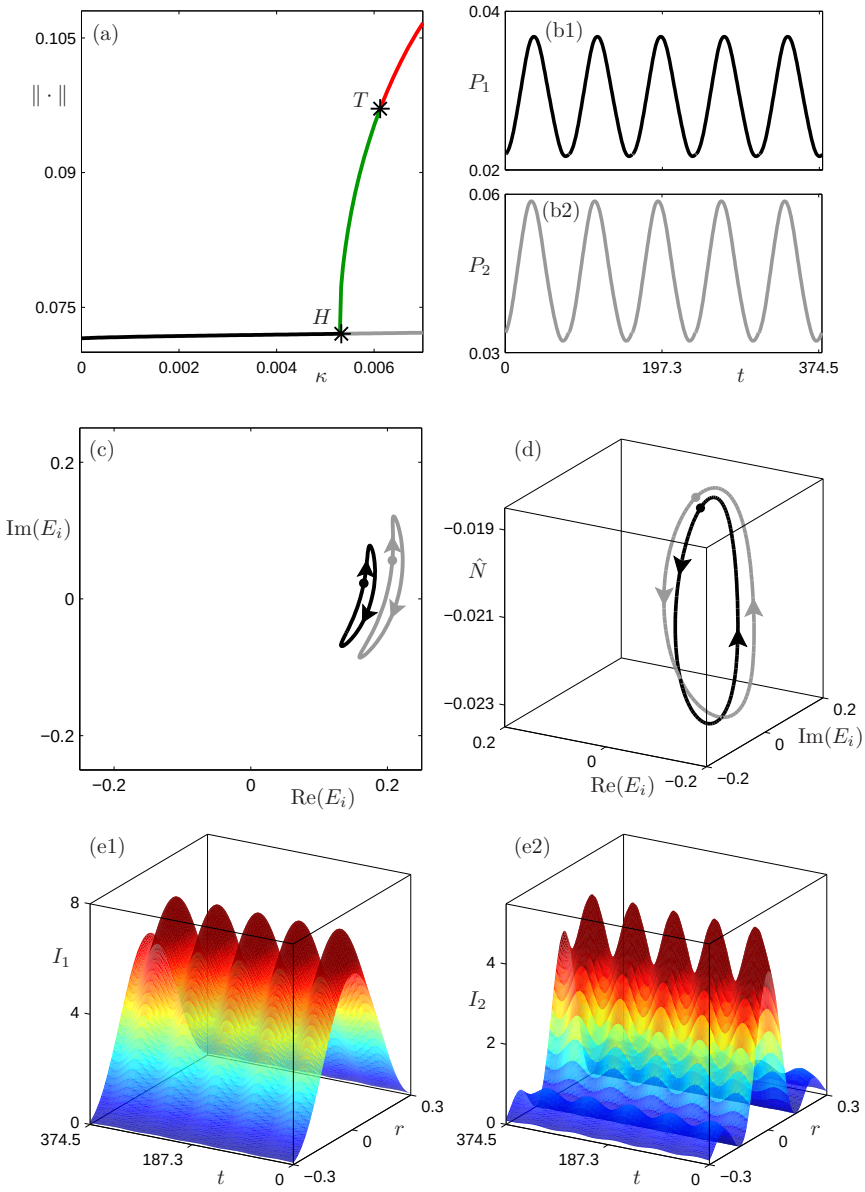

FIG. 6. *The branch of periodic solutions for $\eta = 0.6$ emanating from the Hopf bifurcation curve H_{11} in Fig. 5(a), and the stable periodic solution for $\kappa = 0.006$ (b)–(e). Panels (b1) and (b2) show the time series of the powers P_1 and P_2 of the two modes, panels (c) and (d) are projections onto the E_i-plane and $(E_i, \hat{N})$-space, respectively, and panels (e1) and (e2) are time series of the spatial intensities I_1 and I_2. Quantities concerning E_1 are plotted black and quantities concerning E_2 are plotted gray; throughout $C_p = 0$.*

solutions emanating from H_{12} and H_{22} have a period of approximately 640 time units (781 MHz), and those emanating from H_{13} and H_{23} have a period of approximately 400 time units (1.25 GHz). We remark that a switch between in-phase and anti-phase dynamics, as the pump current was increased, was shown to occur in a similar VCSEL

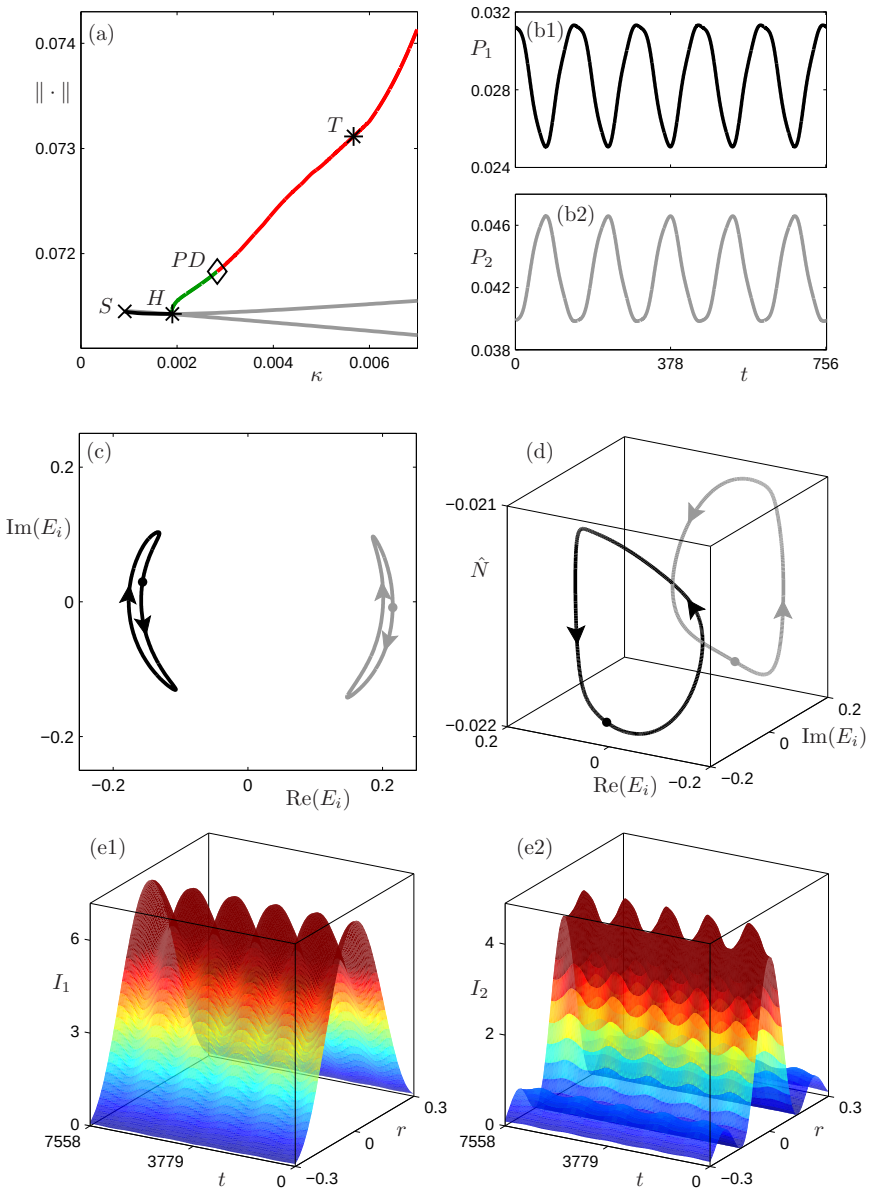

FIG. 7. *The branch of periodic solutions for $\eta = 0.2$ emanating from the Hopf bifurcation curve H_{31} in Fig. 5(c). The stable periodic solution for $\kappa = 0.0025$ is presented in panels (b)–(e) in the same projections as in Fig. 6.*

model [43].

4.1. Stability regions of periodic solutions. Figure 8 shows the stability regions of periodic solutions in the (κ, η)-plane. They were found with `PDDE-CONT` by detecting, and then continuing in κ and η, saddle-node of limit cycle bifurcations SL (brown), period-doubling bifurcations PD (green), and torus bifurcations T (black). The curves (red) of Hopf bifurcations of ECMs are reproduced from Fig. 5. Specifically,

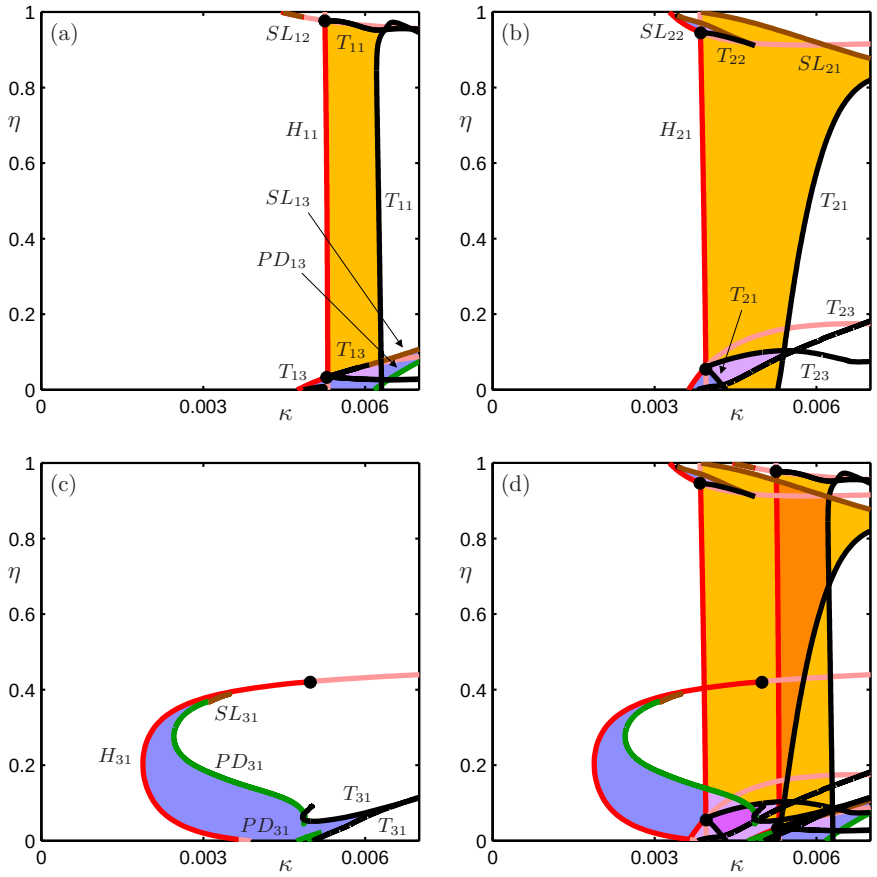

FIG. 8. *Stability regions of different periodic solutions in the (κ, η)-plane, which are bounded by curves of Hopf bifurcation (red), saddle-node bifurcations of limit cycle bifurcation (brown), period-doubling bifurcation (green), and torus bifurcation (black). Stability regions of in-phase ROs are shaded yellow, and that of anti-phase EOs are shaded blue. Panel (d) is an overlay of the different stability regions in panels (a)–(c), where coloring indicates regions of multistability; throughout $C_p = 0$.*

Figs. 8(a) and (b) show the stability regions (orange) of the in-phase ROs that are born at the Hopf curves H_{11}, H_{12}, H_{13} identified in Fig. 5(a), and H_{21}, H_{22}, H_{23} identified in Fig. 5(b), respectively. Furthermore, Fig. 8(c) shows the stability regions (blue) of the anti-phase external round trip oscillations that are born at the Hopf curve H_{31} identified in Fig. 5(c). Regions shaded purple indicate bistability between in-phase and anti-phase solutions. The final panel, Fig. 8(d), shows the complete stability diagram of periodic orbits in the (κ, η)-plane; namely, it is an overlay of panels (a) to (c). Regions are shown in different shades of color to indicate coexistence between different stable periodic solutions.

Figure 8(a) shows that, for most values of cross-coupling η, the stable in-phase ROs emanating from H_{11} are destabilized, as κ is increased, in a torus bifurcation T_{11} (black curve); compare with Fig. 6(a). For large η there are additional curves of torus bifurcations emanating from a double-Hopf point, which can be crossed by changing

η for fixed κ. The situation for small η is even more complicated, with additional torus, saddle-node of limit cycle and period-doubling curves bounding the stability region of the anti-phase oscillations emanating from H_{13}. In fact, the interplay of these bifurcation curves, which are associated with another double-Hopf point, leads to a small region of bistability between the in-phase and anti-phase periodic solutions born at the Hopf curves H_{11} and H_{13}, respectively; this region is indicated in Fig. 8(a) by purple shading. The situation shown in Fig. 8(b), for the in-phase ROs emanating from H_{21}, is very similar. They exist stably in a large region of the (κ, η)-plane, covering effectively the entire η-range. When κ in increased, these periodic solutions are destabilized in torus bifurcations T_{21} (black curve) over almost the entire η-range, namely for approximately $\eta < 0.8$, and in a saddle-node of limit cycle bifurcation SL_{21} (brown curve) for approximately $\eta > 0.8$. Again, the situation is a bit more complicated for large and small η due to additional bifurcation curves that are connected to double-Hopf points; as a result a small purple region of bistability between in-phase and anti-phase solutions is again created for $\eta < 0.1$.

As Fig. 8(c) shows, the blue stability regions of the anti-phase EOs born at the Hopf curve H_{31} is quite different. The region itself is much smaller and can be found only for large cross-coupling, namely for $\eta < 0.4$. For most values of η these oscillations are destabilized in a period-doubling bifurcation; compare with Fig. 7(a). However, for $\eta < 0.1$ we find destabilization in a torus bifurcation T_{31}, and for $\eta \approx 0.4$ there is a small curve SL_{31} of saddle-node bifurcations of limit cycles. The latter curve is in fact associated with a curve of homoclinic bifurcations that emanates from the saddle-node Hopf point; the homoclinic dynamics of the modes is discussed in the next section.

Overall, Figs. 5 and 8 represent the stability information of all ECMs and the periodic solutions emanating from their Hopf bifurcations that can be found for weak feedback κ and any level of self- versus cross-coupling η. The considerable amount of multistability between the different types of solutions can be inferred from the combination of Figs. 5(f) and 8(d).

5. Beyond stable periodic solutions. As we have seen, periodic solutions lose their stability when κ is increased beyond the respective stability regions. Interestingly, the in-phase ROs destabilize mainly in torus bifurcations, while the prominent EOs destabilize in period-doubling bifurcations; see Fig. 8. We now consider the ensuing dynamics in more detail, where we start from the periodic solutions identified in Figs. 6 and 7, respectively.

Figure 9 shows two-frequency dynamics for $\eta = 0.6$. Panel (a) is a bifurcation diagram where for each value of κ the maximum and minimum of the trajectory of the first mode (in black) and the second mode (in gray) are plotted, after transients have died out. The computation was started from the periodic solution for $\kappa = 0.006$ from Fig. 6 so that its bifurcations are tracked. We find the Hopf bifurcation at $\kappa \approx 0.0053$, in which this periodic solution is born from the stable ECM, and the torus bifurcation at $\kappa \approx 0.0063$; compare with Fig. 5(a). Indeed for $\kappa > 0.0063$ the dynamics takes place on an invariant torus that manifests itself in the bifurcation diagram of Fig. 9(a) as large blocks of points. The dynamics on the torus appears to be quasiperiodic or of very high period. This is confirmed in Figs. 9(b) to (d), where the solution for $\kappa = 0.0065$ is shown as time series of the powers, and projections onto the E_i-plane and $(E_i, \hat{N})$-space. Note that the two electric fields E_1 and E_2 still oscillate in phase with the RO period, while their amplitudes are also modulated by a slowly varying envelope with period close to the external cavity round trip time. Figures 9(e1) and

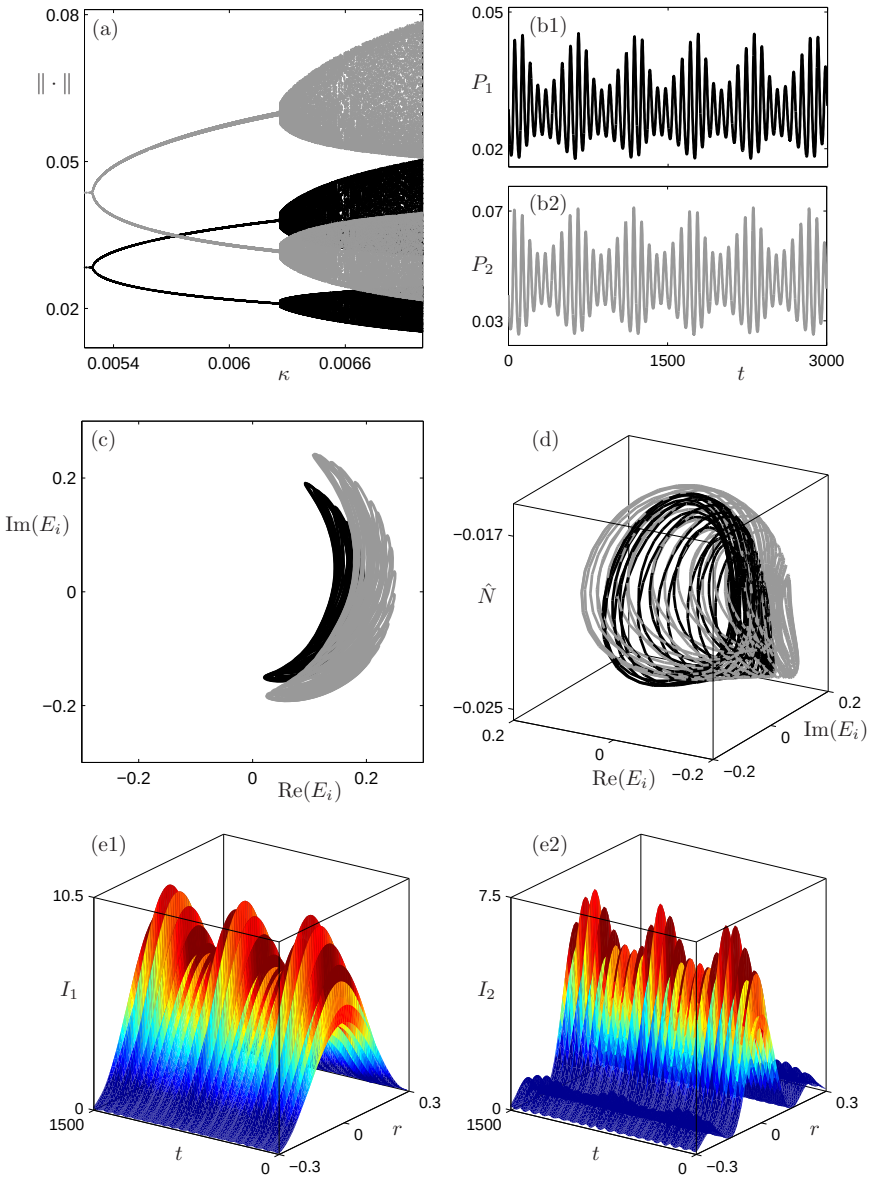

FIG. 9. *Bifurcation to an in-phase torus for $\eta = 0.6$ with increasing κ (a). Stable quasiperiodic dynamics for $\kappa = 0.065$ is presented in panels (b)–(e) as in Figs. 6 and 7.*

(e2) show how this two-frequency dynamics manifests itself in terms of the spatial intensities I_1 and I_2 of the two modes. Notice that the fast oscillations are clearly seen in the flanks of the intensity profiles.

Figure 10 shows chaotic anti-phase dynamics for $\eta = 0.2$. The bifurcation diagram in panel (a) was started from the periodic solution for $\kappa = 0.0025$ from Fig. 7. One recognizes the Hopf bifurcation from the stable ECM at $\kappa \approx 0.0019$ and the first period-doubling at $\kappa \approx 0.00283$; compare with Fig. 7(a). It emerges that this period-

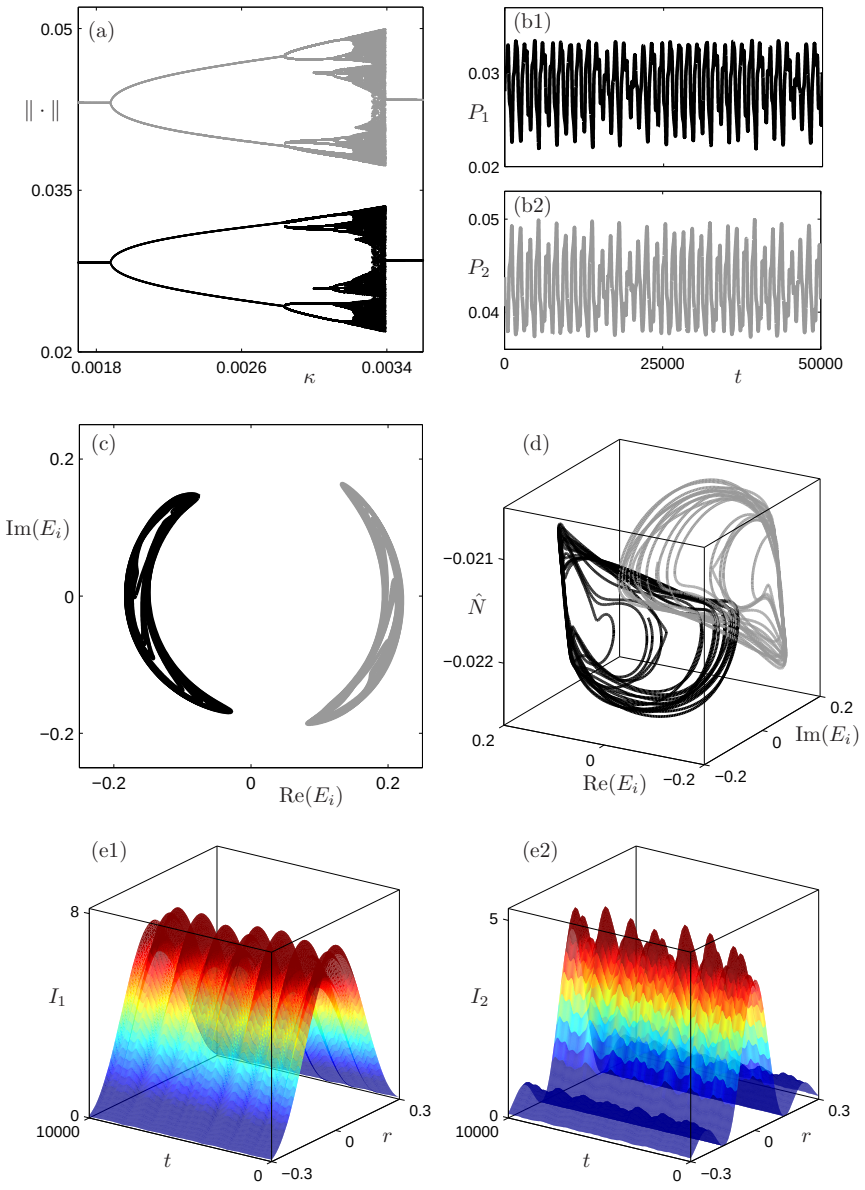

FIG. 10. *Period doubling to an anti-phase chaotic attractor for* $\eta = 0.2$ *with increasing* κ *(a). Chaotic dynamics for* $\kappa = 0.00338$ *is presented in panels (b)–(e) as in Figs. 6 and 7.*

doubling is the first in a classic period-doubling route to chaos. Figures 10(b) to (d) show the chaotic solution for $\kappa = 0.00338$ as time series of the powers and projections onto the E_i-plane and $(E_i, \hat{N})$-space. Note from panels (b1) and (b2) that the chaotic dynamics of the individual modes are in anti-phase. As for the periodic solution from which it bifurcated, panels (c) and (d) show that the projections onto the two electric fields E_1 and E_2 are located about π out of phase; compare with Figs. 7(c) and (d). Note further, that the mean fluctuations of the chaotic dynamics are on the

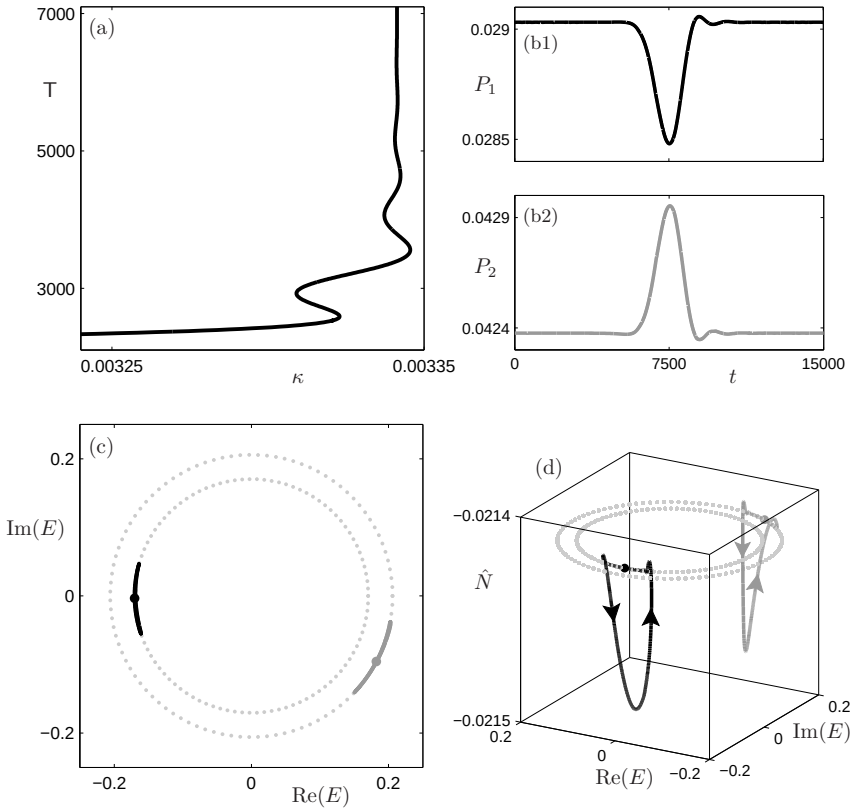

FIG. 11. *Branch of periodic solutions converging to a homoclinic orbit for* $\eta = 0.39$ *(a), and the approximate homoclinic orbit for* $\kappa \approx 0.003341$ *as a series (b), in* E_i*-plane (c), and in* $(E_i, \hat{N})$*-space (d); throughout* $C_p = 0$.

time-scale of the period of the underlying periodic solution, namely, about three times τ. Figures 10(e1) and (e2) show the chaotic dynamics as time series of the spatial intensities I_1 and I_2 of the two modes. The chaotic dynamics is particularly evident in the flanks of the intensity profiles.

The saddle-node Hopf point SNH in Figs. 5(c) and 8(c) gives rise to homoclinic orbits of the underlying ECM. Such a homoclinic orbit is shown in Fig. 11. It was found by continuing the branch of anti-phase EOs for $\eta = 0.39$ in the feedback strength κ. Panel (a) shows this branch plotted in terms of the period T. It folds back and forth while T goes to infinity when κ converges to $\kappa \approx 0.003341$ – a clear indication of a homoclinic orbit at this parameter value. This is confirmed by the time series of the powers P_1 and P_2 of the periodic orbit for $\kappa = 0.003341$ that approximates the homoclinic orbit; see Figs. 11(b1) and (b2). The approximate homoclinic orbit itself is shown in projections onto the E_i-plane and $(E_i, \hat{N})$-space in panels (c) and (d), respectively. Here we also show (as dotted circles) the unstable ECM (in terms of both fields) to which the periodic orbit becomes homoclinic. Note the anti-phase nature of the time series, which is inherited from the underlying anti-phase EO. The power $P_i = |E_i|^2$ of the individual modes is very small; this can be concluded from the fact that the projection of the periodic orbit onto the E_i-plane does not 'leave' the

ECM circles; see Fig. 11(c). Therefore, the spatial mode profiles remain practically constant at the ECM level, which is why they are not shown in Fig. 11.

6. Conclusions and outlook. We have considered the dynamics of spatially extended transverse optical modes of a vertical cavity surface emitting laser subject to optical feedback as modeled by delayed partial differential equations (DPDEs). By means of an eigenfunction expansion we derived a set of delay differential equations (DDEs) describing the interaction of any number of optical modes. In this general formulation the number of equations that need to be retained after truncation of the expansion depends on which and how many optical modes one wishes to consider, which is determined by the physical size of the VCSEL. The ensuing system of DDEs is quite small when compared with that obtained by a discretization of the spatial part of the DPDE with a finite difference scheme. Furthermore, the overlap integrals that determine the spatial coupling between the optical modes can be computed off-line and then appear as constants in the system of DDEs. The combination of these two properties resulted in a substantial gain in the numerical efficiency of the model, so that a multi-parameter bifurcation analysis of the mode-expanded DDE model with specialized software tools is now feasible.

With this approach we studied the case of a VCSEL that supports the two (rotationally symmetric) fundamental optical modes LP_{01} and LP_{02}, which are coupled via the external feedback. A bifurcation analysis of the resulting mode-expanded 18-dimensional DDE model, describing the spatial dynamics in terms of the radial mode profile of the VCSEL, was performed with the numerical continuation tools `DDE-BIFTOOL` and `PDDE-CONT`. A comparison with a finite difference discretization scheme [14] confirmed the accuracy of this model on the level of one-parameter bifurcation diagrams of the steady-state external cavity modes. We then computed the stability of the ECMs in dependence on the feedback strength κ and the self- versus cross-coupling parameter η. This revealed regions of coexisting, stable ECMs in the (κ, η)-plane, which are bounded by curves of saddle-node and Hopf bifurcations. The bifurcating periodic solutions may be in-phase relaxation oscillations (ROs) or anti-phase external round trip oscillations (EOs). Both were shown to occur stably in large regions of the (κ, η)-plane. We finally considered how these periodic solutions may bifurcate to more complicated dynamics. In particular, this revealed that the VCSEL with optical feedback may display chaotic spatio-temporal dynamics, which is of potential interest for chaotic communication schemes [35].

Overall, our bifurcation analysis clearly shows the importance of the self- versus cross-coupling parameter η for the dynamics of the spatial modes. While the case of pure self-feedback is degenerate, for an intermediate level of cross-feedback in the range $\eta \in [0.4, 0.9]$ we identified a typical bifurcation scenario when the feedback strength κ is increased: additional ECMs are born in saddle-node bifurcations; stable ECMs lose their stability in Hopf bifurcations, in which stable in-phase ROs are born; these oscillations then give rise to two-frequency dynamics on an invariant torus, where the new modulation frequency is due to the external round trip of the light. In the range $\eta < 0.4$, that is, for larger levels of cross-feedback, we find stable anti-phase EOs where the two fields suppress each other. When κ is increased, the anti-phase EOs destabilize in a cascade of period-doublings that eventually results in anti-phase spatio-temporal chaos. Physically, one sees a chaotic switching between the two modes. The clear distinction between in-phase ROs and anti-phase EOs may provide a means of determining the level of cross-feedback in an experiment. Furthermore, the challenge is to record spatially resolved measurements of VCSEL

modes on a picosecond time scale; this may be possible with the techniques developed in Refs. [1, 2].

There are several directions for future research. First of all, the question arises what happens when the VCSEL supports more than the two fundamental modes LP_{01} and LP_{02}. The mode-expanded DDE model can be used to describe the interaction between any number of transverse optical modes, but it becomes increasingly involved. The next physically relevant case arises when the first higher-order mode LP_{11} is involved in the dynamics as well. Already in this situation, which still concerns a VCSEL with quite a small aperture, the dynamics can no longer be described solely by the radial mode profile. This effectively doubles the dimension of the mode-expanded DDE model, and is presently under investigation. Secondly, as soon as higher-order transverse modes are involved, one may also wish to consider the interaction between the spatial modes and the polarization. Again, this doubles the dimension of the model. Finally, the mode expansion presented here can also be used to model other (laser) systems that combine spatial extent with delays. Obvious examples are VCSELS with filtered or phase-conjugate optical feedback or mutual delay-coupling, and broad area lasers subject to optical feedback.

Acknowledgments. We thank Robert Szalai for help with `PDDE-CONT`. The research of K.G. was financially supported under the Dynamics of Patterns Program of the Netherlands Organization for Scientific Research (NWO) and the Foundation for Fundamental Research on Matter (FOM).

REFERENCES

[1] A. Barchanski, T. Genstry, C. Degen, I. Fischer and W. Elsässer, *Picosecond Emission Dynamics of Vertical-Cavity Surface-Emitting Lasers: Spatial, Spectral, and Polarization-Resolved Characterization*, IEEE Quantum Elec., 39:850–858, 2003.

[2] K. Becker, I. Fischer and W. Elsässer, *Spatio-Temporal Emission Dynamics of VCSELs: Modal Competition in the Tun-On Behavior*, Proc. of SPIE, 5452:452–461, 2004.

[3] W. F. Brinkmann and D. V. Lang, *Physics and the communications industry*, Rev. Mod. Phys., 71:480–488, 1999.

[4] C. Degen, B. Krauskopf, G. Jennemann, I. Fischer and W. Elsässer, *Polarization selective symmetry breaking in the near-fields of vertical cavity surface emitting lasers*, J. Opt. B: Quantum Semiclass. Opt, 2:517–525, 2000.

[5] O. Diekmann, S. A. van Gils, S. M. Verduyn Lunel and H. -O. Walther, *Delay Equations: Functional-, Complex-, and Nonlinear Analysis*, Springer-Verlag, New York, 1995.

[6] E. J. Doedel, R. Paffenroth, A. R. Champneys, T. F. Fairgrieve, Y. A. Kuznetsov, B. E. Oldemann, B. Sandstede and X. Wang, *AUTO 2000: Continuation and Bifurcation Software for Ordinary Differential Equations (with HomCont)*, 2000, `http://cmvl.cs.concordia.ca/auto/`

[7] K. Engelborghs, T. Luzyanina and G. Samaey, *DDE-BIFTOOL v. 2.00: a Matlab package for bifurcation analysis of delay differential equations*, Technical Report TW-330, Department of Computer Science, K.U.Leuven, Leuven, Belgium, 2001.

[8] K. Engelborghs and D. Roose, *On stability of LMS methods and characteristic roots of delay differential equations*, SIAM J. Numer. Anal., 40:629–650, 2002.

[9] H. Erzgräber, B. Krauskopf, and D. Lenstra, *Bifurcation analysis of a semiconductor laser with filtered optical feedback*, SIAM J. Applied Dynamical Systems, 6(1):1–28, 2007.

[10] H. Erzgräber, D. Lenstra, B. Krauskopf, A. P. A. Fischer and G. Vemuri, *Feedback phase sensitivity of a semiconductor laser subject to filtered optical feedback: experiment and theory*, `http://hdl.handle.net/1983/916`, 2007.

[11] I. Fischer, T. Heil, and W. Elsässer, *Emission dynamics of semiconductor lasers subject to delayed optical feedback: an experimentalists perspective*, Fundamental Issues of Nonlinear Lasers Dynamics (B. Krauskopf and D. Lenstra; Eds.), American Institute of Physics, 2000, pp. 218–237.

[12] K. Green, B. Krauskopf and G. Samaey, *A two-parameter study of the locking region of a semiconductor laser subject to phase-conjugate feedback*, SIAM J. Applied Dynamical Systems, 2(2):254–276, 2003.

[13] K. Green and B. Krauskopf *Bifurcation analysis of a semiconductor laser subject to non-instantaneous phase-conjugate feedback*, Opt. Commun., 231:383–393, 2004.

[14] K. Green, B. Krauskopf and D. Lenstra, *External cavity mode structure of a two-mode VCSEL subject to optical feedback*, Opt. Commun., 277:359–371, 2007.

[15] J. Guckenheimer and P. Holmes, *Nonlinear Oscillations, Dynamical Systems, and Bifurcations of Vector Fields*, Springer-Verlag, New York, 1983.

[16] B. Haegeman, K. Engelborghs, D. Roose, D. Pieroux, and T. Erneux, *Stability and rupture of bifurcation bridges in semiconductor lasers subject to optical feedback*, Phys. Rev. E, 66(046216), 2002.

[17] J. Hale and S. M. Verduyn Lunel, *Introduction to Functional Differential Equations*, Springer-Verlag, New York, 1993.

[18] R. N. Hall, G. E. Fenner, J. D. Kingsley, T. J. Soltys and R. O. Carlson, *Coherent light emission from GaAs junctions*, Phys. Rev. Lett., 9:366–369, 1962.

[19] T. Heil, I. Fischer, W. Elsässer, and A. Gavrielides, *Dynamics of semiconductor lasers subject to delayed optical feedback: The short cavity regime*, Phys. Rev. Lett., 87 (2001), p. 243901.

[20] T. Heil, I. Fischer, W. Elsässer, B. Krauskopf, K. Green and A. Gavrielides, *Delay dynamics of semiconductor lasers with short external cavities: bifurcation scenarios and mechanisms*, Phys. Rev. E, 67(066214), 2003.

[21] M. X. Jungo, D. Erni and W. Bächtold, *VISTAS: A Comprehensive System-Oriented Spatiotemporal VCSEL Model*, IEEE Sel. Topics in Quantum Elec., 9:939–948, 2003.

[22] D. M. Kane and K. A. Shore, *Unlocking Dynamical Diversity: Optical Feedback Effects on Semiconductor Lasers*, Wiley, 2005.

[23] H. Kawaguchi, *Bistabilities and Nonlinearities in Laser Diodes*, Artech House, Boston, 1994.

[24] B. Krauskopf, *Bifurcation analysis of lasers with delay*, Unlocking Dynamical Diversity: Optical Feedback Effects on Semiconductor Lasers (D. M. Kane and K. A. Shore; Eds), Wiley, 2005, pp. 147-183.

[25] B. Krauskopf and D. Lenstra, *Fundamental Issues of Nonlinear Lasers Dynamics*, American Institute of Physics, 2000.

[26] B. Krauskopf, G. H. M. Van Tartwijk, and G. R. Gray, *Symmetry properties of lasers subject to optical feedback*, Opt. Commun., 177:347–353, 2000.

[27] Y.N. Kyrychko, S.J. Hogan, A. Gonzalez-Buelga, and D.J. Wagg, *Modelling real-time dynamic substructuring suing partial delay differential equations*, Proc. R. Soc. A 463:1509-1523, 2007.

[28] R. Lang and K. Kobayashi, *External Optical Feedback Effects on Semiconductor Injection Laser Properties*, IEEE Quantum Elec., 16:347–355, 1980.

[29] J. Y. Law and G. P. Agrawal, *Effects of Optical Feedback on Static and Dynamic Characteristics of Vertical-Cavity Surface-Emitting Lasers*, IEEE Sel. Topics in Quantum Elec., 3:353–358, 1997.

[30] J. Y. Law, G. H. M. van Tartwijk and G. P. Agrawal, *Effects of transverse-mode competition on the injection dynamics of vertical-cavity surface-emitting lasers*, Quantum Semiclass. Opt., 9:737–747, 1997.

[31] D. Lenstra, B. H. Verbeek, and A. J. den Boef, *Coherence collapse in single-mode semiconductor lasers due to optical feedback*, IEEE J. Quantum Electron., 21(6):674–679, 1985.

[32] F. Marino, S. Barland and S. Balle, *Single-Mode Operation and Transverse-Mode Control in VCSELs Induced by Frequency-Selective Feedback*, IEEE Photonics Tech. Lett., 15(6):789–791, 2003.

[33] J. Martin-Regalado, S. Balle, M. San Miguel, A. Valle, and L. Pesquera, *Polarization and transverse-mode selection in quantum-well vertical-cavity surface-emitting lasers: index- and gain-guided devices*, Quantum Semiclass. Opt., 9:713–736, 1997.

[34] K. Moriki, H. Nakahara, T. Hattori, and K. Iga, *Single Transverse Mode Condition of Surface-Emitting Injection Lasers*, Elec. Commun. Japan, 71(1):81–90, 1988.

[35] J. García-Ojalvo and R. Roy, *Spatiotemporal communication with synchronized optical chaos*, Phys. Rev. Lett., 86:5204–5207, 2001.

[36] Y. Onishi, N. Nishiyama, C. Caneau, F. Koyama and C.-E. Zah, *All-Optical Regeneration Using Transverse Mode Switching in Long-Wavelength Vertical-Cavity Surface-Emitting Lasers*, Jpn. J. Appl. Phys., 45(17):467–468, 2006.

[37] M. Sciamanna, K. Panajotov, H. Thienpont, I. Veretennicoff, P. Mégret and M.

Blondel, *Optical feedback induces polarization mode hopping in vertical-cavity surface-emitting lasers*, Opt. Lett., 28(17):1543–1545 (2003).

[38] M. Sciamanna, T. Erneux, F. Rogister, O. Deparis, P. Mégret and M. Blondel, *Bifurcation bridges between external-cavity modes lead to polarization self-modulation in vertical-cavity surface-emitting lasers*, Phys. Rev. A, 65:041801(R), 2004.

[39] G. Stepán, *Retarded Dynamical Systems: Stability and Characteristic Functions*, Longman Scientific and Technical, London, UK, 1989.

[40] R. Szalai, *PDDE-CONT: A continuation and bifurcation software for delay-differential equations*, Budapest University of Technology and Economics, Hungary, 2005, `http://www.mm.bme.hu/~szalai/pdde`

[41] D. Roose and R. Szalai, *Continuation and bifurcation analysis of delay differential eqautions*, Numerical Continuation Methods for Dynamical Systems: Path following and boundary value problems (B. Krauskopf, H. M. Osinga and J. Galn-Vioque; Eds.), Springer-Verlag, 2007, pp. 359–399.

[42] C.M. Topaz, J. Porter, and M. Silber, *Multifrequency control of Faraday wave patterns*, Phys. Rev. E 70:066206, 2004.

[43] M. S. Torre, C. Masoller and P. Mandel, *Transverse-mode dynamics in vertical-cavity surface-emitting lasers with optical feedback*, Phys. Rev. A, 66:053817, 2002.

[44] A. Valle, *Selection and modulation of high-order transverse modes in vertical-cavity surface-emitting lasers*, IEEE J. Quantum Electron., 34(10):1924–1932, 1998.

[45] K. Verheyden, T. Luzyanina and D. Roose, *Efficient computation of characterisitc roots of delay differential equations using LMS methods*, J. Comput. Appl. Math., in press, 2007.

[46] S. F. Yu, *Analysis and Design of Vertical Cavity Surface Emitting Lasers*, Wiley, 2003.